Numerical Simulation of Flow-Induced Birefringence: Comparison of Injection and Injection/Compression Molding

Ho-Sang Lee[1,#] and A. I. Isayev[2]

1 Department of Aeronautical & Mechanical Design Engineering, Chungju National University, Chungju, Chungbuk, South Korea
2 Institute of Polymer Engineering, University of Akron, Akron, Ohio 44325-0301, USA
Corresponding Author / E-mail: lhs@chungju.ac.kr; Tel: +82-43-841-5375; Fax: +82-43-841-5370

KEYWORDS: Injection/Compression molding, Viscoelastic simulation, Velocity, Pressure, Birefringence

A computer code was developed to simulate the filling stage of an injection/compression molding process using a finite element method. The constitutive equation was the compressible Leonov model and the PVT relationship was assumed to follow the Tait equation. The flow-induced birefringence was related to the calculated flow stresses through the linear stress-optical law. Simulations of a disk under different processing conditions, including variations of the compression stroke and compression speed, were performed to determine their effects on the flow-induced birefringence. Simulated pressure traces were also compared to those obtained in conventional injection molding and with experimental data from the literature.

Manuscript received: January 9. 2006 / Accepted: July 14, 2006

1. Introduction

The importance of molding processes to manufacture precision plastic optical parts, such as lenses, disk substrates, and other optical components, is continuously increasing. Plastics offer significant advantages compared to conventional optical glass parts. Besides their light weight and lower material loss, a further advantage of injection molded polymer optical products is the integration of the mounting and assembly features, such as brackets or snap-fit-joints, which can be molded with the optical element in a one-shot process. Several special injection molding techniques have been developed to fulfill the rising requirements on the parts for quality. One of these techniques, injection/compression molding, is a widely used process. By adding a compression stage after partial melt filling of the cavity, molded parts with a lower molecular orientation can be manufactured at a lower pressure.[1] The optical part quality strongly depends on the internal part properties, such as molecular orientation. Thus, injection/compression molding offers the opportunity to manufacture high-precision optical parts with improved optical quality.

Klepek[2] used injection/compression molding to mold thick optical lenses. Yang *et al.*[3-5] experimentally investigated the quality of disks molded using injection/compression molding. They showed that injection/compression molding enhanced the dimensional accuracy, especially in the direction perpendicular to the compression. Michaeli and Wielpuetz[6] investigated main processing parameters influencing the optical part quality in the injection/compression molding process, using a design of experiments. In their experiments, the main influencing parameters on the optical part quality were the injection and compression velocity for injection/compression as well as the injection velocity and packing pressure for conventional injection molded parts. At the present time, a science-based design technique for injection/compression molding of optical products has not been established. This is due to a lack of understanding of the viscoelastic mechanical and optical behavior of polymeric materials during cavity filling of injection stage and squeezing flow occurring during compression stage.

Numerical analysis of the process that includes the viscoelastic effects is quite difficult. Isayev and Hieber[7] were among the first to propose a theoretical approach to relate the nonlinear viscoelasticity of polymers to the development of the frozen-in molecular orientation (birefringence) in injection moldings. Isayev and Azari[8] and Isayev *et al.*[9] performed both theoretical and experimental investigations of the squeezing flow of the melt using nonlinear viscoelastic constitutive equations. They considered a shear-free flow and channel flow with a moving boundary squeezing melt, similar to what occurs during the compression stage of molding. Osswald and Tucker[10] presented a compression molding simulation for non-planar parts that combined a finite element solution of the governing equations with a control volume scheme for tracking the moving flow front based on inelastic flow models. The simulation results were compared with those of experiments, including both model laboratory materials and production SMC moldings. Kim *et al.*[11] and Lee *et al.*[12] developed a numerical analysis system based on a finite difference method for the governing equations of the symmetric radial flow and studied the distribution of birefringence in a center-gated disk after injection and injection/compression molding using the Leonov model.[13] They showed that injection/compression molding could reduce birefringence compared with injection molding. Chen *et al.* performed inelastic[14,15] and viscoelastic[16] numerical analyses of the injection/compression molding process. Although they studied the effects of the averaged birefringence variation under various processing parameters, the gapwise birefringence distribution was

Copyright (c) 2007 by KSPE

not described. Recently, Fan *et al.*[17] developed a code for simulating injection/compression molding of a CD-R using a compressible viscous flow model. Comparisons between the measured and calculated nozzle pressures and the mold displacement were made.

In this study, we develop a numerical flow simulation program for an injection/compression molding process using the finite element method. The constitutive equation used here is the compressible Leonov model.[13] The PVT relationship is assumed to follow the Tait equation.[18] Using the linear stress-optical law,[19] the flow-induced birefringence is related to the flow stresses calculated with the Leonov model. Simulated pressure profiles of both injection and injection/compression molding are compared with experimental data from the literature to verify the numerical predictions. In addition, simulations of a disk under different processing conditions, including variations of the compression stroke and compression speed, are performed to determine their effects on the birefringence variation. Simulated pressure traces are also compared to those obtained for conventional injection molding.

2. Finite Element Analysis

2.1 Governing Equations

There are two mold filling stages during an injection/compression molding process: partial injection mold filling with a polymeric melt into a slightly open mold, and the subsequent compression mold filling by complete closing of the mold. Inelastic[20] and viscoelastic[21] simulations of the injection stage have already been developed based on the control volume approach. Here, the governing equations for the compression stage are given.

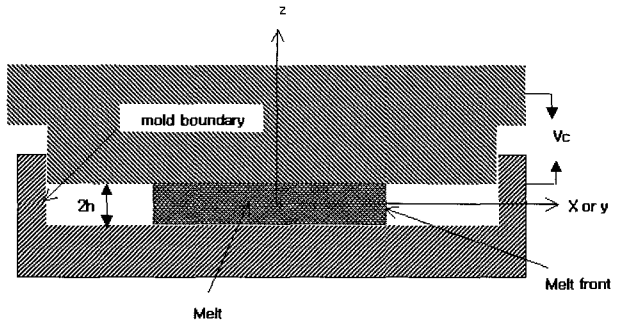

Fig. 1 Schematic diagram of compression molding

Using the coordinate system shown in Fig. 1, the momentum equations in the absence of inertia and body forces are

$$\frac{\partial \sigma_{xx}}{\partial x}+\frac{\partial \sigma_{xz}}{\partial z}=0 \tag{1}$$

$$\frac{\partial \sigma_{yy}}{\partial y}+\frac{\partial \sigma_{yz}}{\partial z}=0 \tag{2}$$

$$\frac{\partial \rho}{\partial t}+\frac{\partial}{\partial x}(\rho v_x)+\frac{\partial}{\partial y}(\rho v_y)+\frac{\partial}{\partial z}(\rho v_z)=0 \tag{3}$$

where x and y are the planar directions, z is the gapwise direction, σ_{ij} represents the total stress, and v_x, v_y, and v_z are the velocity components in the x, y, and z directions, respectively. The density ρ is assumed to follow the Tait equation.[18]

$$\rho(P,T)=\rho_0(T)\left\{1-C\ln\left[1+\frac{P}{B(T)}\right]\right\}^{-1} \tag{4}$$

where C is a constant and B is a function of temperature.

In a nonisothermal problem, the momentum and continuity equations are coupled with the energy equation. Then the energy equation is

$$\rho C_p\left(\frac{\partial T}{\partial t}+v_x\frac{\partial T}{\partial x}+v_y\frac{\partial T}{\partial y}\right)=\frac{\partial}{\partial z}\left(\kappa\frac{\partial T}{\partial z}\right)+\Phi \tag{5}$$

where C_p, κ, and Φ are the specific heat, thermal conductivity, and dissipation function, respectively.[13]

By employing the Leonov constitutive model,[13] the stress field can be related to the velocity gradient field as follows:

$$\underline{\underline{\sigma}}=-P\underline{\underline{\delta}}+\eta_0 s(\nabla \underline{v}+\nabla \underline{v}^T)+\sum_k \frac{\eta_k}{\theta_k}\underline{\underline{C_k}} \tag{6}$$

where P is the pressure, s is a rheological parameter lying between zero and one, and η_k, θ_k, and C_k are the shear viscosity, relaxation time, and elastic strain tensor for the k^{th} mode of the Leonov model.

The boundary conditions may be summarized as:

$$v_x=v_y=0,\ v_z=-v_c \text{ at } z=h \tag{7}$$

$$\frac{\partial v_x}{\partial z}=\frac{\partial v_y}{\partial z}=0 \text{ at } z=0 \tag{8}$$

$$P=0 \text{ at the melt front} \tag{9}$$

$$Q=Q_0 \text{ at the gate or entry} \tag{10}$$

$$T=T_w \text{ at } z=h \tag{11}$$

$$\frac{\partial T}{\partial z}=0 \text{ at } z=0 \tag{12}$$

By substituting Eq. 6 into Eqs. 1 and 2 and integrating the results with respect to z using the symmetric boundary condition (Eq. 8), the velocity gradients in the absence of normal forces are

$$\frac{\partial v_x}{\partial z}=\frac{\partial P}{\partial x}\frac{z}{\eta_x} \tag{13}$$

$$\frac{\partial v_y}{\partial z}=\frac{\partial P}{\partial y}\frac{z}{\eta_y} \tag{14}$$

where

$$\eta_x=\eta_0 s+\frac{1}{\frac{\partial v_x}{\partial z}}\sum_k\frac{\eta_k}{\theta_k}C_{xz,k} \tag{15}$$

$$\eta_y=\eta_0 s+\frac{1}{\frac{\partial v_y}{\partial z}}\sum_k\frac{\eta_k}{\theta_k}C_{yz,k} \tag{16}$$

The integration of Eqs. 13 and 14 using Eq. 7 leads to

$$v_x=-\frac{\partial P}{\partial x}\int_z^h\frac{z'}{\eta_x}dz' \tag{17}$$

$$v_y=-\frac{\partial P}{\partial y}\int_z^h\frac{z'}{\eta_y}dz' \tag{18}$$

By substituting Eqs. 17 and 18 into Eq. 3, the governing equation for pressure is

$$G\frac{\partial P}{\partial t}+H-\frac{\partial}{\partial x}\left(S_x\frac{\partial P}{\partial x}\right)-\frac{\partial}{\partial y}\left(S_y\frac{\partial P}{\partial y}\right)-\rho_{z=h}v_c=0 \tag{19}$$

where

$$G=\int_0^h\left(\frac{\partial \rho}{\partial P}\right)dz \tag{20}$$

$$H=\int_0^h\left(\frac{\partial \rho}{\partial T}\right)\left(\frac{\partial T}{\partial t}\right)dz \tag{21}$$

$$S_x=\int_0^h\left(z\int_z^h\rho\,dz'\right)\frac{dz}{\eta_x} \tag{22}$$

$$S_y = \int_0^h (z \int_0^z \rho dz') \frac{dz}{\eta_y} \tag{23}$$

The trol-volume finite element method[20,21] with triangular elements and linear shape functions is used to solve Eq. 19. G and H are assumed constant in each control volume and S_x and S_y are assumed constant in each element. For general planar geometries, the elastic strain tensor is determined in the streamwise coordinate system (r, θ, z), where r is the flow direction, θ is perpendicular to r in the counterclockwise direction, and z is the gapwise direction. The numerical scheme used to solve the elastic strain tensor is described in Refs. 22–24.

The flow-induced birefringence in the rz plane can be calculated from the stress-optical law[19] as

$$\Delta n = C_\sigma^{fl} \sqrt{(\sigma_{rr} - \sigma_{zz})^2 + 4\tau_{rz}^2} \tag{24}$$

where C_σ^{fl} is the stress-optical coefficient at the melt state.

2.2 Melt Front Advancement in the Compression Stage

The volumetric flow rate of the melt during the compression stage is equal to the rate at which the closing mold displaces the volume occupied by the filling process through the surface defined by the melt front boundaries. The filling parameter associated with each control volume is taken into consideration using the mass flux from the moving surface. For control volumes located on the flow front, the filling parameter can be calculated from the occupied volume fraction and the additional volume fraction due to compression during a specified instant.

The total mass flow rate of the melt through the surface during the compression stage is

$$Q_c = 2\frac{\sum_i \rho_i f_i V_i}{2h_k} v_c \tag{25}$$

where h_k is the half-thickness at time $t = k$, and f_i and V_i are the filling parameter and volume of control volume i.

Using the pressure gradient, the mass flow rate q_{Ni} from element N into control volume i can be calculated by assuming a constant velocity over the element. By equating the new mass of material in control volume i at time $t = k + 1$ to the sum of the old mass at time $t = k$ and the mass flow into the control volume during Δt, the filling parameter f_i for each node can be calculated from

$$\rho_i^{k+1} f_i^{k+1} V_i^{k+1} = \rho_i^k f_i^k V_i^k + \sum_N q_{Ni} \Delta t \tag{26}$$

For each control volume i, the mass at time $t = k$ is

$$\rho_i^k V_i^k = \rho_{avg} \sum_N \frac{A_{Ni}}{3} 2h^k \tag{27}$$

where ρ_{avg} is the density averaged along the thickness and A_{Ni} is the area of triangular element N connected with node i. The mass at time $t = k + 1$ is

$$\rho_i^{k+1} V_i^{k+1} = \rho_{avg} \sum_N \frac{A_{Ni}}{3} 2(h^k - v_c \Delta t) \tag{28}$$

By substituting Eqs. 27 and 28 into Eq. 26 and setting $f_i^{k+1} = 1$, the time increment Δt_i required to fully fill the control volume at node i is

$$\Delta t_i = \frac{\rho_{avg}(1 - f_i^k) \sum_N \frac{A_{Ni}}{3} 2h^k}{\sum_N (q_{Ni} + 2v_c \frac{A_{Ni}}{3} \rho_{avg})} \tag{29}$$

The time increment is calculated for every melt front node and the smallest value is selected as the next time increment. From Eqs. 26 – 28, the filling parameter at every melt front node can be updated as follows:

$$f_i^{k+1} = \frac{f_i^k h^k}{h^k - v_c \Delta t} + \frac{\sum_N q_{Ni} \Delta t}{\rho_{avg} \sum_N \frac{A_{Ni}}{3} 2(h^k - v_c \Delta t)} \tag{30}$$

During the compression stroke, the numerical simulation of the injection mold filling for a partially opened mold is performed as described in Ref. 22. When the amount of injected melt inside the cavity is exactly the same as the required final part volume, the process is switched to the compression stage. The computational domain during the transient compression stage is updated by changing the location of the melt front and the half-gap thickness of the cavity with a time step for the melt front advancement using Eqs. 29 and 30. The simulation is performed until the mold cavity is completely filled, which is determined by checking the filling parameters.

3. Material and Procedures

The simulation was based on the experiment and input data of Chen *et al.*[15] The material used is Polystyrene (CHI MEI/PG33) and the mold is a center-gated disk. The diameter and thickness of the disk is 14 cm and 0.1 cm, respectively. The molding conditions are as follows: a melt temperature of 240°C, a mold temperature of 40°C, a volumetric flow rate of 76.6 cm^3/s, a compression stroke of 0.05 cm, and a compression speed of 1.0 cm/s. Based on the C-MOLD database, the model parameters of the Leonov viscoelastic equation were calculated using a least square fitting method. The data for the polystyrene material used in the simulation are listed in Table 1. A total of 315 elements with 184 nodes are used to model a quarter disk, considering the symmetry of the disk. The amount of melt injected inside the cavity before compression was defined so that the volume of the material would be exactly the same as the part volume.

Simulations were also conducted for other experimental conditions used by Chen *et al.*[15] These conditions are shown in Table 2. The thickness of the disk and volumetric flow rate were 0.2 cm and 156 cm^3/s, respectively, while the other conditions were the same as those described above.

Table 1 Properties of Polystyrene CHI MEI/PG33

- Leonov Model Parameters at T_o = 462.977 K with N = 6 and s = 0.0005:
  $\eta_1(T_o)$ = 10234.6 Pa·s, $\theta_1(T_o)$ = 10 s
  $\eta_2(T_o)$ = 10211.1 Pa·s, $\theta_2(T_o)$ = 0.8 s
  $\eta_3(T_o)$ = 2272.9 Pa·s, $\theta_3(T_o)$ = 0.0644 s
  $\eta_4(T_o)$ = 188.4 Pa·s, $\theta_4(T_o)$ = 0.00517 s
  $\eta_5(T_o)$ = 65.1 Pa·s, $\theta_5(T_o)$ = 0.000415 s
  $\eta_6(T_o)$ = 1.69 Pa·s, $\theta_6(T_o)$ = 0.000033 s
- Parameters in WLF equation:
  C_1 = 25.878, C_2 = 51.6, T_{ref} = 373.15 K
- Glass transition temperature: T_g = 378 K
- Stress-optical coefficient: $C_\sigma^{fl} = -4.8 \times 10^{-9} Pa^{-1}$
- Thermal conductivity: κ = 0.18 J / m·s·K
- Specific heat: $C_p = 2.10 \times 10^3$ J / kg·K

Table 2 Processing parameters

Processing parameters	Case A	Case B	Case C
Compression stroke (cm)	0.05	0.1	0.1
Compression speed (cm/s)	2.0	2.0	1.0

4. Results and Discussion

4.1 Pressure and Temperature Development

Fig. 2 compares the simulated cavity pressure near the gate at the end of the filling stage with the corresponding experimental data reported by Chen *et al.*[15] for both conventional injection molding (CIM) and injection/compression molding (ICM). The predicted pressure profiles are in good agreement with the experimental results. However, there are some differences in the magnitude near the switching time of 0.20 s. A possible reason may be the response-time delay of approximately 0.025 s for switching the injection/compression molding machine to the compression mode.

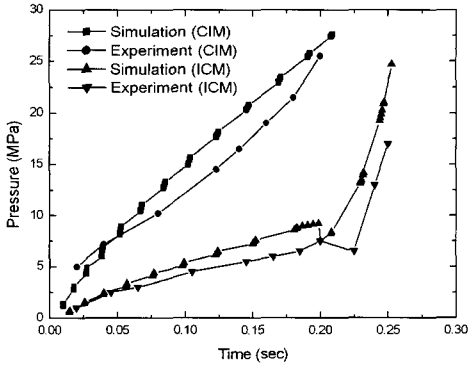

Fig. 2 Comparison of predicted cavity pressure profiles near the gate with experimental data measured by Chen *et al.* [15] for CIM and ICM

As expected, the pressure at various radial positions differed significantly in injection molding, as shown in Fig. 3. This difference was smaller in injection/compression molding, as shown in Fig. 4, although the pressure abruptly increased when the mold closed during the compression stage. From Fig. 5, a slight additional decrease in the pressure difference was obtained as the compression stroke increased. The thicker cavity gap in larger mold openings reduced the temperature drop slightly during the filling stage, as shown in Fig. 6, resulting in a relatively more uniform pressure inside the cavity. The pressure decreased in magnitude with decreasing compression speed, as shown in Fig. 7. This can be explained by considering the relatively reduced normal force when the mold closed at the lower compression speed. These results indicate that the pressure became more uniform over the entire cavity and decreased in magnitude with increasing compression strokes and decreasing compression speeds.

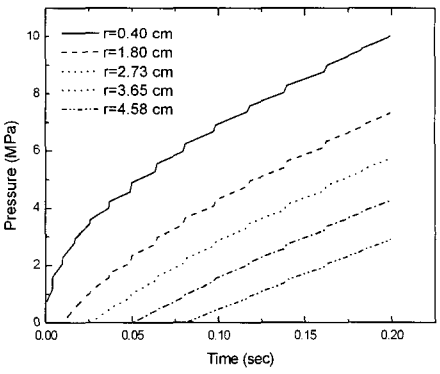

Fig. 3 Simulated pressure traces at various radial positions during the filling stage of injection molding

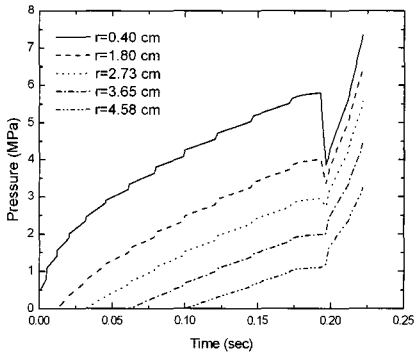

Fig. 4 Simulated pressure traces at various radial positions during the injection and compression stages of injection/ compression molding under Case A conditions

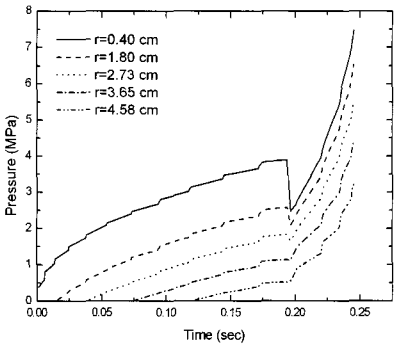

Fig. 5 Simulated pressure traces at various radial positions during the compression stage of injection/compression molding under Case B conditions

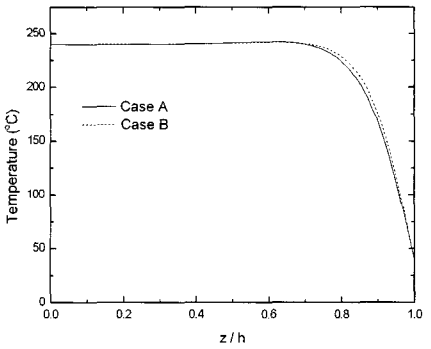

Fig. 6 Gapwise distribution of temperature at a radial position of 4.58 cm at the end of compression during injection/compression molding under Case A and Case B conditions

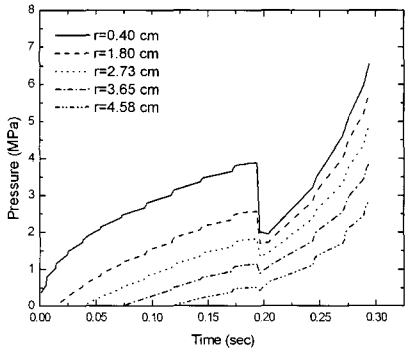

Fig. 7 Simulated pressure traces at various radial positions during the injection and compression stages of injection/compression molding under Case C conditions

4.2 Velocity Profiles

Fig. 8 shows the predicted gapwise velocity profiles at the end of filling during injection molding. As expected, the velocity decreased with increasing radial positions from the gate and the melt flow diminished around $z / h = 0.8$ due to cooling from the mold wall. However, the velocity increased with the radius during injection/compression molding, as shown in Fig. 9. Similar velocity profiles were also obtained in Refs. 11 and 16. The velocity behavior can be explained by considering the mass balance. Since the volumetric flow rate of the melt through the surface increased with the radius, the velocity through the section at a position far from the gate was greater than that near the gate due to the mass balance. In addition, the centerline velocity difference between $r = 1.80$ cm and $r = 4.58$ cm was 60 cm/s in conventional injection molding (see Fig. 8), whereas the value was only 21 cm/s in injection/compression molding (see Fig. 9). This is an indication that the squeezing flow during the compression stage causes the pressure distribution in the mold cavity to become more uniform, resulting in a reduction of the flow velocity difference with position.

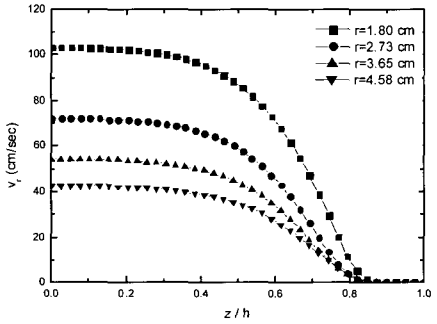

Fig. 8 Predicted gapwise distribution of velocity v_r at various radial positions at the end of filling during injection molding ($t = 0.21$ s)

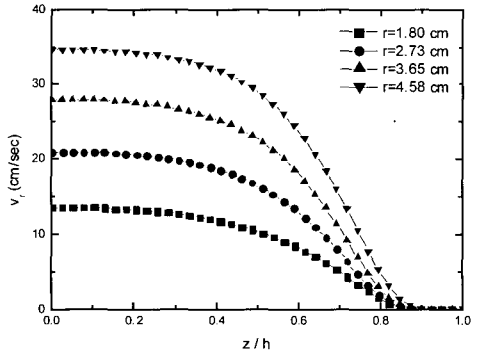

Fig. 9 Predicted gapwise distribution of velocity v_r at various radial positions at the end of the compression stage ($t = 0.222$ s) during injection/compression molding under Case A conditions

4.3 Birefringence Development

The predicted gapwise flow birefringence distribution at various radial positions at the end of the filling stage during injection molding is shown in Fig. 10. The maximum birefringence occurred at $z / h = 0.85 - 0.90$ due to the dominant effect of the first normal stress difference. The peaks continually decreased in magnitude with increasing radial position from the gate.

It is important to identify the effects of the compression stage on the birefringence in molded parts. For this purpose, numerical simulations were performed using the varying compression strokes and compression speeds listed in Table 2. Figs. 11–13 show the predicted gapwise birefringence distribution during injection/compression molding. The birefringence peaks increased with the radius, the opposite of the results obtained during injection molding (see Fig. 10). This tendency could be caused by the different velocity profiles described above. From these figures, it is clear that the introduction of a compression stage after partial melt filling of the cavity reduced the level of birefringence. The birefringence was reduced slightly as the compression stroke became larger. Although a larger stroke increased the effects of the compression stage slightly and reduced the stresses due to the relatively low cavity pressure described above, it did not significantly reduce the birefringence, as noted in the simulation results reported in Refs. 11 and 16. Our simulation results are in agreement with the experimental data in Ref. 16: both sets of data indicate similar small effects of the compression stroke on the birefringence.

As the compression speed decreased, the birefringence also decreased in magnitude and became more uniform over the entire cavity, as shown in Figs. 12 and 13. This could be because the slower material flow through the surface defined by the melt front boundaries at low compression speeds causes a decrease in the shear rate, resulting in a lower birefringence. This is also in agreement with the experimental results of Ref. 16: both sets of data indicate that the compression speed significantly affects the birefringence distribution in moldings. Therefore, we conclude that one of the main parameters affecting the quality of an optical part in injection/compression molding is the compression speed, as observed in the experiments of Michaeli and Wielpuetz[6]. The birefringence is significantly lower and more uniform in injection/compression molding than in injection molding. The quality of optical parts strongly depends on the frozen-in birefringence. Therefore, injection/compression molding processes offer the opportunity to manufacture high-precision optical parts with improved optical quality.

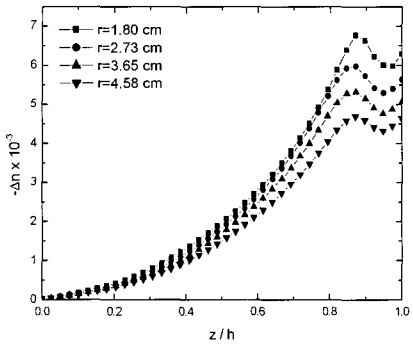

Fig. 10 Predicted gapwise distribution of the birefringence Δn at various radial positions at the end of filling during injection molding ($t = 0.21$ s)

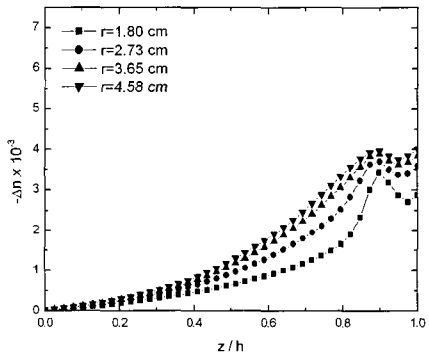

Fig. 11 Predicted gapwise distribution of the birefringence Δn at various radial positions at the end of the compression stage ($t = 0.222$ s) during injection/compression molding under Case A conditions

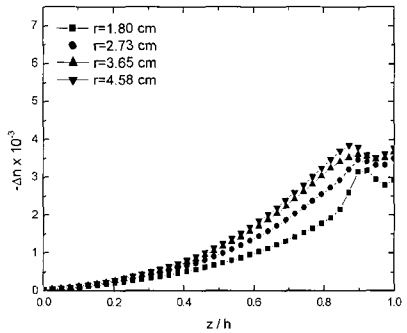

Fig. 12 Predicted gapwise distribution of the birefringence Δn at various radial positions at the end of the compression stage (t = 0.246 s) during injection/compression molding under Case B conditions

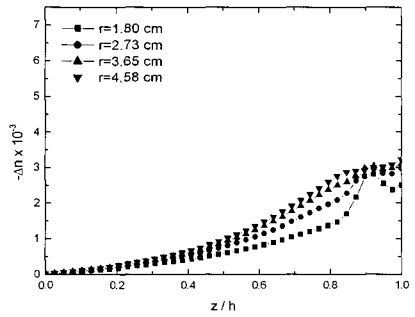

Fig. 13 Predicted gapwise distribution of the birefringence Δn at various radial positions at the end of the compression stage (t = 0.294 s) during injection/compression molding under Case C conditions

5. Conclusions

A numerical flow simulation program using a finite element method for injection/compression molding was developed. The constitutive equation used here was the compressible Leonov model. The PVT relationship was assumed to follow the Tait equation. The flow-induced birefringence was related to the flow stresses calculated by the Leonov model using the linear stress-optical law. To verify the numerical predictions, simulated pressure profiles for both injection molding and injection/compression molding were compared with experimental data from the literature. In addition, simulations of a partial disk using different process conditions, including varying compression strokes and compression speeds, were performed to determine their effects on the birefringence variation.

The predicted pressure profiles were in good agreement with the experimental results. However, there were some differences in the pressure magnitude when the simulation switched from an injection to a compression process due to the time delay introduced when switching the injection/compression molding machine to the compression stage. The velocity increased with the radius of the cavity during injection/compression molding. This result was the opposite of the trend during injection molding. Also, the cavity pressure was reduced in magnitude. The pressure became more uniform over the entire cavity and decreased in magnitude with increasing compression stroke and decreasing compression speed. Therefore, a higher compression stroke and lower compression speed result in lower levels of birefringence. The compression speed particularly affected the flow-induced birefringence distribution. The birefringence during injection/compression molding was lower and more uniform than that obtained during injection molding. Since the quality of an optical part strongly depends on the frozen-in birefringence, injection/ compression molding offers the opportunity to manufacture high-precision optical parts with improved optical quality.

ACKNOWLEDGEMENT

This work was supported by Chungju National University research grants in 2005.

REFERENCES

1. Isayev, A. I., "Molding Processes, in Handbook of Industrial Automation," Marcel Dekker, New York, pp. 573-606, 2000.
2. Klepek, G., "Manufacturing Optical Lens by Injection Compression Molding," Kunststoffe, Vol. 77, p. 13, 1987.
3. Yang, S. Y. and Chen, Y. C., "Experimental Study of Injection-Charged Compression Molding of Thermoplastic," Advances in Polymer Technology, Vol. 17, pp. 353-360, 1998.
4. Yang, Y. and Ke, M. Z., "Experimental Study of Injection Compression Molding," Proc. SPE ANTEC'93, pp. 2182-2187, 1993.
5. Yang, S. Y. and Ke, M. Z., "Experimental Study on the Effects of Adding Compression to Injection Molding Process," Advances in Polymer Technology, Vol. 14, pp. 15-24, 1995.
6. Michaeli, W. and Wielpuetz, M., "Optimization of the Optical Quality of Polymer Glasses in the Injection Compression Molding Process," Macromol. Mater. Eng., Vol. 284/285, pp. 8-13, 2000.
7. Isayev, A. I. and Hieber, C. A., "Toward a Viscoelastic Modeling of the Injection Molding of Polymers," Rheol. Acta., Vol. 19, pp. 168-182, 1980.
8. Isayev, A. I. and Azari, A. D., "Viscoelastic Effect in Compression Molding of Elastomers: Shear-Free Squeezing Flow," Rubber Chemistry and Technology, Vol. 59, pp. 868-882, 1986.
9. Isayev, A. I., Zhang, Y. and Zook, C., "Advances in the Flow and Rheology of Non-Newtonian Fluids," Balkema Publishers, Rotterdam, pp. 1011-1067, 1999.
10. Osswald, T. A. and Tucker, C. L., "Compression Mold Filling Simulation for Non-Planar Parts," Intern. Polymer Processing V, pp. 79-87, 1990.
11. Kim, I. H., Park, S. J., Chung, S. T. and Kwon, T. H., "Numerical Modeling of Injection/Compression Molding for Center-Gated Disk: Part II. Effect of Compression Stage," Polym. Eng. Sci., Vol. 39, pp. 1943-1951, 1999.
12. Lee, Y. B., Kwon, T. H. and Yoon, K., "Numerical Prediction of Residual Stresses and Birefringence in Injection/Compression Molded Center-Gated Disk: Part 2. Effects of Processing Conditions," Polym. Eng. Sci., Vol. 42, pp. 2273-2292, 2002.
13. Shyu, G. D. and Isayev, A. I., "Residual Stresses and Birefringence in Injection Molded Disks," SPE ANTEC Tech Papers, Vol. 41, pp. 2911-2916, 1995.
14. Chen, S. C., Chen, Y. C. and Cheng, N. T., "Simulation of Injection-Compression Mold-Filling Process," Int. Comm. Heat Mass Transfer, Vol. 25, pp. 907-917, 1998.
15. Chen, S. C., Chen, Y. C. and Peng, H. S., "Simulation of Injection-Compression-Molding Process, Part 2: Influence of Process Characteristics in Part Shrinkage," Appl. Polym. Sci., Vol. 75, pp. 1640-1654, 2000.
16. Chen, S. C., Chen, Y. C. and Peng, H. S., "Simulation of Injection-Compression-Molding Process, Part 3: Effect of Process Conditions on Part Birefringence," Advance in Polymer Technology, Vol. 21, pp. 177-187, 2002.
17. Fan, B. and Kazmer, D. O., "Simulation of Injection-Compression Molding for Optical Media," Polym. Eng. Sci., Vol. 43, pp. 596-606, 2003.
18. Tait, P. G., "Physics and Chemistry of the Voyage of H.M.S. Challenger," Scientific Papers LXI, Vol. 2, No. 4, 1988.
19. Janeschitz-Kriegl, H., "Polymer Melt Rheology and Flow

Birefringence," Springer, Berlin, 1983.
20. Wang, V. W., Hieber, C. A. and Wang, K. K., "Dynamic Simulation and Graphics for the Injection Molding of Three-Dimensional Thin Parts," J. Polym. Eng., Vol. 7, pp. 21-45, 1986.
21. Isayev, A. I., ed., "Modeling of Polymer Processing: Recent Developments," Hanser, Munich, 1991.
22. Shyu, G. D., Isayev, A. I. and Lee, H. S., "Residual Stresses and Birefringence in Injection Molded Disks," Korea-Australia Rheology J., Vol. 15, pp. 159-166, 2003.
23. Sobhanie, M. and Isayev, A. I., "Viscoelastic Simulation of Flow of Rubber Compounds," Rubb. Chem. Tech., Vol. 62, pp. 939-956, 1989.
24. Han, S., Huh, Y. J. and Kang, S., "Optimum Design of Process Conditions to Minimize Residual Stress and Birefringence," International Journal of Precision Engineering and Manufacturing, Vol. 2, No. 2, pp. 17-25, 2001.